

# Hamiltonian dynamics for stochastic reconstruction in emission tomography

T Leontiou<sup>1,2,\*</sup>, A Frixou<sup>3</sup>, E Ttof<sup>4,5</sup>, C Chrysostomou<sup>6</sup>, Y Parpottas<sup>1,2</sup>, K Michael<sup>7</sup>, S Frangos<sup>7</sup>, E Stiliaris<sup>3,8</sup> and C N Papanicolas<sup>3,9</sup>

<sup>1</sup>Department of Mechanical Engineering, Frederick University, Nicosia, Cyprus

<sup>2</sup>Frederick Research Center, Nicosia, Cyprus

<sup>3</sup>CaSToRC, The Cyprus Institute, Nicosia, Cyprus

<sup>4</sup>Department of Electrical and Computer Engineering and Informatics, Frederick University, Nicosia, Cyprus

<sup>5</sup>Information Technology Department, German Medical Institute, Limassol, Cyprus

<sup>6</sup>ERATOSTHENES Centre of Excellence, Cyprus University of Technology, Limassol, Cyprus

<sup>7</sup>Bank of Cyprus Oncology Center, Nicosia 2006, Cyprus

<sup>8</sup>Department of Physics, National and Kapodistrian University of Athens, Athens, Greece

<sup>9</sup>The Cyprus Academy of Sciences, Letters and Arts

\*Author to whom any correspondence should be addressed.

**E-mail:** t.leontiou@frederick.ac.cy

**Keywords:** emission tomography, SPECT, Hamiltonian Monte Carlo, stochastic gradient descent, uncertainty quantification, inverse problems

---

## Abstract

The AMIAS/RISE framework formulates emission tomography as a probabilistic inverse problem in which reconstructed images are sampled from a distribution defined by the measurement model and counting statistics. In this work we present a stochastic reformulation of this approach based on gradient-driven optimization combined with Hamiltonian Monte Carlo (HMC) sampling directly in high-dimensional voxel space. This formulation enables practical ensemble generation for tomographic image reconstructions and provides direct access to image fluctuations within the sampled ensemble. Beyond point reconstruction, we introduce a spatially resolved operator-weighted diagnostic—the sampled data-visible variance—which quantifies how image fluctuations propagate through the imaging operator and thereby probes the local conditioning of the inverse problem under realistic acquisition physics. Using controlled software phantoms, experimental anthropomorphic phantom measurements, and a clinical DATSCAN SPECT acquisition, we demonstrate that while point-estimate accuracy under ideal conditions is comparable to deterministic reconstruction methods, the stochastic formulation provides additional physically interpretable insight. In particular, the ensemble analysis distinguishes uncertainty arising from intrinsic ill-posedness of the inverse problem from that associated with forward-model inadequacy. The clinical example is included to illustrate methodological applicability under realistic acquisition statistics rather than to assess diagnostic performance. The results establish the stochastic reconstruction framework as a practical ensemble-based approach for uncertainty quantification and forward-model validation in emission tomography.

---

## 1 Introduction

Emission tomography poses a computationally intensive inverse problem: reconstructing the spatial distribution of radiotracer activity from projection data that are incomplete, noisy, and affected by physical processes, including photon attenuation and scattering. To place this challenge in context, the imaging process can be summarized in a series of key steps (Figure 1): 1) a radiotracer is injected into the patient, where it undergoes uptake by tissues and radioactive decay with  $\gamma$ -ray emission; 2) the emitted photons propagate through the body, undergoing attenuation and scattering; 3) photons are detected by a collimated gamma camera, which restricts their directionality; 4) the detected counts are organized into projection data, known as sinograms; 5) finally, the inverse problem is solved to reconstruct the underlying radiotracer distribution from the measured sinograms.

Traditionally, image reconstruction has relied on deterministic iterative methods such as Maximum Likelihood Expectation Maximization (MLEM) or Ordered Subsets Expectation Maximization (OSEM) and their variants [1]. These approaches aim to obtain a point estimate of the activity distribution by maximizing the Poisson likelihood or, equivalently, minimizing a data-fidelity objective derived from counting statistics.

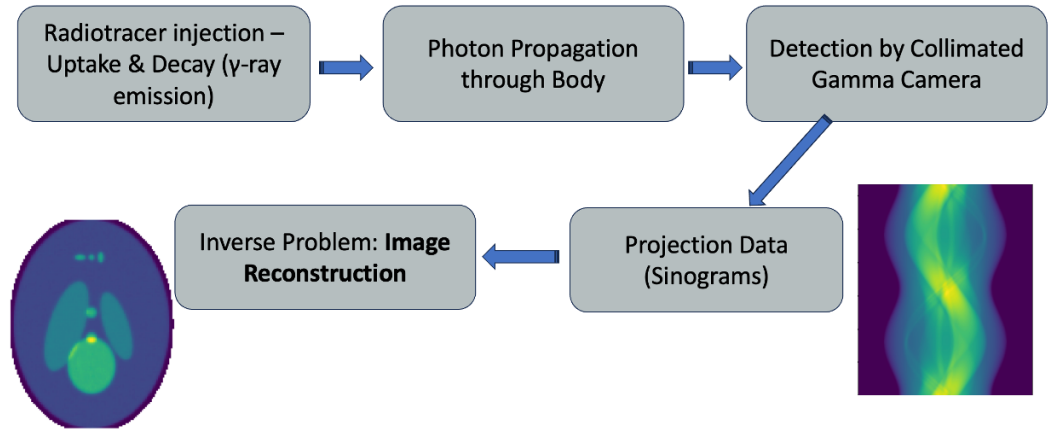


Figure 1: Key steps of the emission tomography process: radiotracer administration and photon propagation, detection and projection data formation, and the final inverse reconstruction problem.

A different perspective on the inverse problem was introduced with the Athens Model Independent Analysis Scheme (AMIAS) [2, 3]. AMIAS formulates reconstruction as a statistical inference problem, generating ensembles of solutions that satisfy a forward model and assigning each a probability based on a  $\chi^2$  measure of agreement with the data. This formulation defines a probability density function (PDF) over the model parameters, enabling estimation of both best-fit values and associated uncertainties. Originally developed in hadronic physics [4, 5, 6], AMIAS has since been adapted to medical imaging [7].

For tomographic imaging, AMIAS was extended into the Reconstructed Image from Simulations Ensemble (RISE) method [8], in which voxel intensities are treated as parameters of a multivariable PDF and probabilities are assigned to entire reconstructed images based on their consistency with measured projections. RISE has been successfully applied in SPECT [9, 10], PET [11], and infrared emission tomography [12], demonstrating competitive image quality and providing uncertainty information through ensemble analysis [13].

While the original AMIAS/RISE implementations demonstrated the conceptual advantages of ensemble-based reconstruction, their computational structure made practical application challenging for large voxel spaces or full three-dimensional reconstructions. In the present work, we reformulate the AMIAS/RISE framework using modern stochastic optimization and Hamiltonian Monte Carlo sampling directly in voxel space. This reformulation enables practical generation of image ensembles for full three-dimensional reconstructions and, crucially, provides access to ensemble-based diagnostics that reveal how reconstruction uncertainty interacts with the measurement physics.

In parallel, recent years have witnessed rapid progress in machine learning-based reconstruction methods for emission tomography [14, 15]. These approaches have demonstrated substantial gains in computational speed and image quality through data-driven training and hardware-optimized implementations, and are increasingly attractive for clinical deployment. However, many such methods are designed primarily to produce a single reconstructed image and do not explicitly sample the underlying probability distribution, which can limit direct assessment of reconstruction uncertainty and of forward-model adequacy.

The stochastic ensemble framework considered here is not intended to replace deterministic or learning-based approaches, but rather to provide a physically interpretable probabilistic layer through which reconstruction uncertainty and model consistency can be quantitatively assessed.

In this work, reconstruction is formulated within a Hamiltonian Monte Carlo (HMC) framework. HMC generates samples by simulating classical Hamiltonian dynamics, where auxiliary momentum variables and symplectic integration are used to efficiently explore a given high-dimensional probability distribution. While HMC is well established in statistical computation and in lattice field theory, its systematic use as a primary voxel-space reconstruction engine in emission tomography remains limited.

To improve convergence and computational practicality, stochastic gradient descent (SGD) is employed as a fast deterministic optimizer to locate a high-probability region of the target distribution. The resulting solution serves as initialization for subsequent Hamiltonian sampling, promoting stable and efficient exploration of this high-dimensional space.

The ensemble of images generated by HMC provides physically interpretable diagnostics of the interaction between image fluctuations and the measurement operator. By analyzing ensemble

variability in data-weighted directions, one can assess whether residual uncertainty arises from intrinsic ill-posedness or from limitations of the forward model. At the same time, HMC enables evaluation of reconstructed images and derived observables—such as comparative activity between regions of interest—as expectation values, naturally providing both mean estimates and uncertainty bounds.

The principal contributions of this work are therefore:

- Efficient voxel-space implementation of AMIAS/RISE: A stochastic reformulation that enables practical ensemble generation for full three-dimensional emission tomography using modern tensor-based numerical frameworks.
- Application of Hamiltonian Monte Carlo as a reconstruction engine: Reconstruction is performed through simulation of classical Hamiltonian dynamics, providing a physics-motivated sampling mechanism for high-dimensional probability distributions.
- Forward-model assessment via ensemble diagnostics: The generated image ensembles are used to quantify how fluctuations propagate through the measurement operator, enabling structured evaluation of forward-model adequacy beyond global residual metrics.
- Quantitative estimation of observables: Once an adequate forward model is specified, physical observables—including regional activity measures and image-derived ratios—can be evaluated directly from the generated ensemble, yielding both estimates and statistically consistent uncertainty bounds.

The methodology is demonstrated using controlled software phantoms, experimental anthropomorphic phantom data, and clinical DATScan acquisitions. The objective of the present work is not primarily to improve image appearance, but to introduce a physics-based diagnostic framework for assessing forward-model adequacy in emission tomography.

## 2 Materials and Methods

This section presents the methodological framework used for stochastic reconstruction in emission tomography. We first formulate the inverse problem and the associated statistical model used to define the probability distribution of reconstructed images. The Hamiltonian Monte Carlo (HMC) sampling strategy used to explore this distribution is then described, together with the gradient-based optimization procedure employed for initialization. Finally, we introduce the ensemble-based diagnostics used to analyze fluctuations and their interaction with the measurement operator.

### 2.1 Stochastic formulation of the inverse problem in emission tomography

The goal of Single Photon Emission Computed Tomography (SPECT) reconstruction is to estimate the radiotracer distribution  $\mathbf{x}$  within a patient from projection measurements  $\mathbf{y}$  acquired by rotating gamma cameras. A standard discrete forward model is

$$\mathbf{y} = \mathbf{P}\mathbf{x}, \quad (1)$$

where  $\mathbf{P}$  is the projection operator (or projection matrix) encoding the measurement physics, including geometric projection, attenuation, and scatter. Each element  $y_i$  represents the photon count in detector bin  $i$  (indexed over angle and detector position). In practice, photon detection follows Poisson counting statistics [16].

In emission tomography, the measured detector-bin counts are classically modeled through a linear forward operator relating the unknown image to the expected data [16]. In the present work we adopt this same forward-model structure, but formulate the reconstruction probability directly at the level of the measured detector-bin values. Let  $y_i$  denote the measured value in detector bin  $i$ , and let  $\mu_i$  be its exact expectation value. In the moderate-to-high count regime, the central limit theorem implies that the distribution of the measured bin value may be approximated by a Gaussian centered at  $\mu_i$ ,

$$p(y_i | \mu_i) \propto \exp\left(-\frac{(y_i - \mu_i)^2}{2\sigma_i^2}\right). \quad (2)$$

If the forward model is accurate, the expectation value is represented by

$$\mu_i = (\mathbf{P}\mathbf{x})_i, \quad (3)$$

where  $\mathbf{x}$  denotes the unknown image and  $\mathbf{P}$  is the projection operator. Assuming statistical independence between detector bins, the joint likelihood becomes

$$\Pi(\mathbf{y} | \mathbf{x}) \propto \exp\left(-\frac{1}{2} \sum_i \frac{(y_i - (\mathbf{P}\mathbf{x})_i)^2}{\sigma_i^2}\right) \equiv \exp\left(-\frac{1}{2} \chi^2(\mathbf{x})\right), \quad (4)$$

where the proportionality constant is independent of  $\mathbf{x}$  and is omitted in both optimization and sampling. For emission data, the Poisson model of Shepp and Vardi provides the natural connection between the mean and the variance of each detector bin [16]. Accordingly, in the present implementation we use

$$\sigma_i^2 \approx y_i. \quad (5)$$

Furthermore, in the present work, the sampling distribution over images is taken to be  $\Pi(x) \propto \Pi(y | x)$ . Equation (4) is used in two complementary ways:

- **Hamiltonian Monte Carlo (HMC):** HMC is used to sample the unknown image voxels  $\mathbf{x}$  from the probability density function defined by Eq. (4). To enable efficient sampling, auxiliary momentum variables are introduced and Hamiltonian dynamics are simulated numerically. This procedure generates an ensemble of images that can be used to estimate expectation values and quantify uncertainty.
- **Gradient-based optimization (SGD):** the negative log-likelihood associated with Eq. (4) defines a  $\chi^2$  objective, which is minimized using iterative optimizers (e.g. RAdam) to obtain a high-probability point estimate that is also used to initialize HMC.

In both cases, the dimensionality of voxel-based image representations (often exceeding  $10^6$  unknowns in 3D) necessitates efficient evaluation of forward projections and gradients. Our implementation uses tensor-based numerical libraries to accelerate these operations on widely available GPU hardware.

*2.1.1 Hamiltonian Monte Carlo sampling* Hamiltonian Monte Carlo (HMC) is a Markov Chain Monte Carlo technique that uses concepts from classical mechanics [17] to efficiently explore high-dimensional probability distributions and generate ensembles from such distributions [18]. In the context of SPECT, HMC allows sampling from the probability distribution over image estimates  $\mathbf{x}$  defined by Eq. (4).

To enable this sampling, HMC introduces auxiliary momentum variables  $\mathbf{p}$  and defines a Hamiltonian function:

$$H(\mathbf{x}, \mathbf{p}) = U(\mathbf{x}) + K(\mathbf{p}), \quad (6)$$

where the potential energy  $U(\mathbf{x})$  corresponds to the  $\chi^2$  term derived from the negative log-likelihood:

$$U(\mathbf{x}) = \sum_i \frac{(y_i - (\mathbf{P}\mathbf{x})_i)^2}{2(y_i + \epsilon)}, \quad (7)$$

and the kinetic energy is typically chosen as:

$$K(\mathbf{p}) = \frac{1}{2} \mathbf{p}^T M^{-1} \mathbf{p}, \quad (8)$$

with  $M$  the mass matrix, often set to the identity.

The joint distribution is sampled by simulating Hamilton's equations of motion:

$$\frac{d\mathbf{x}}{dt} = \nabla_{\mathbf{p}} H = M^{-1} \mathbf{p}, \quad (9)$$

$$\frac{d\mathbf{p}}{dt} = -\nabla_{\mathbf{x}} H = -\nabla_{\mathbf{x}} U(\mathbf{x}), \quad (10)$$

using the leapfrog integrator. After a number of integration steps, a Metropolis accept/reject step ensures detailed balance. At equilibrium, the generated ensemble follows the probability density defined by Eq. (4). The reconstructed image is obtained as the ensemble expectation value.

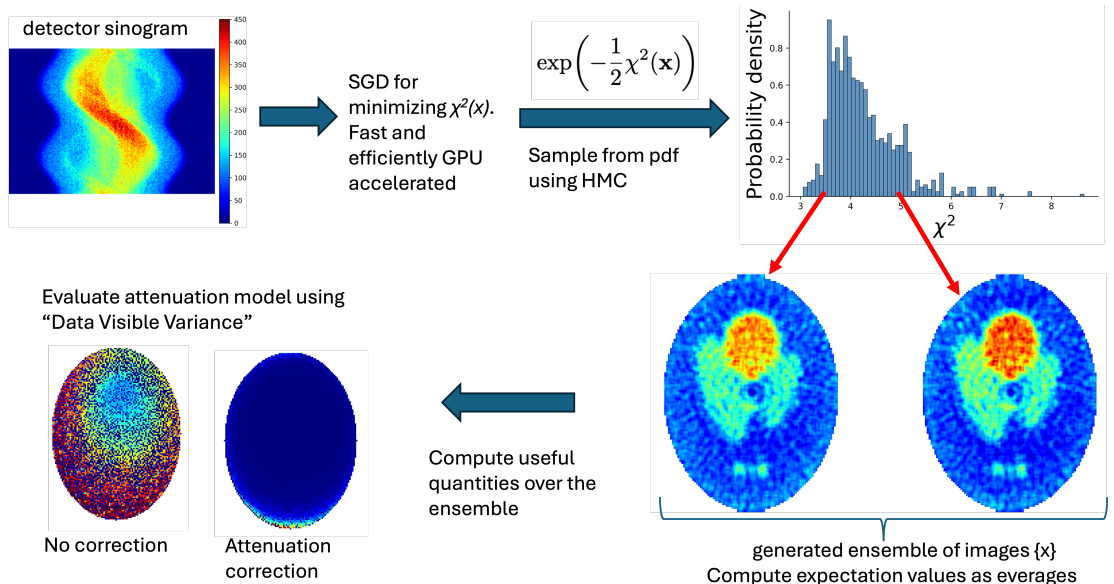


Figure 2: Overview of the stochastic reconstruction workflow and the concept of data-visible variance. Starting from the measured detector sinogram (top left), a probability density over images is defined as  $\Pi(\mathbf{x}) \propto \exp(-\chi^2(\mathbf{x})/2)$  (top middle). A fast gradient-based reconstruction (SGD) is first used to locate a high-probability region of this distribution, providing initialization for Hamiltonian Monte Carlo (HMC) sampling. HMC then generates an ensemble of reconstructed images; the top-right panel illustrates the resulting  $\chi^2$  distribution, and the two example images (bottom right) correspond to representative samples from this ensemble. From the ensemble, voxel-wise statistics can be computed directly in image space. In particular, the data-visible variance is obtained by propagating ensemble fluctuations through the data-weighted projection-backprojection operator  $\mathbf{H} = \mathbf{P}^T \mathbf{W} \mathbf{P}$  (bottom row), thereby isolating the component of variability that remains coupled to the measured data. Comparison of these maps under different forward-model assumptions (e.g. without and with attenuation correction) illustrates how ensemble diagnostics can be used to assess forward-model adequacy beyond global residual measures.

HMC is particularly effective in high-dimensional spaces because it allows for long-range proposals guided by gradients of the log-probability, mitigating the random-walk behavior characteristic of conventional Metropolis–Hastings schemes.

From a physical perspective, HMC treats the reconstruction problem as a statistical mechanical system evolving in an extended phase space. The PDF corresponds to the equilibrium distribution of this system, and Hamiltonian trajectories enable efficient exploration of high-dimensional energy landscapes defined by the data misfit.

The use of HMC in tomographic inverse problems has been demonstrated in [19], including both linear and nonlinear forward models. In the present work, we focus specifically on emission tomography and adapt the HMC formulation to the SPECT measurement model, incorporating Poisson-based weighting, attenuation modeling, and detector/collimator effects encoded in  $\mathbf{P}$ . Our emphasis is not only on sampling efficiency, but on exploiting the resulting ensemble to assess forward-model adequacy under realistic acquisition conditions.

Convergence of the HMC chains was assessed using standard diagnostics, including inspection of trace plots, stabilization of ensemble means, and consistency of variance estimates across independent runs initialized from different starting points. To mitigate potential trapping in local modes, parallel tempering was employed, allowing exchanges between chains at different effective temperatures and facilitating exploration of complex high-dimensional landscapes.

*2.1.2 Data-visible variance from image ensemble* Stochastic reconstruction methods such as Hamiltonian Monte Carlo (HMC) generate an ensemble of images  $\{\mathbf{x}^{(s)}\}_{s=1}^{N_s}$  drawn from the sampling distribution  $\Pi(\mathbf{x})$  defined by Eq. (4). The ensemble contains voxel-wise uncertainty information [13, 20]. For example, the sample mean and variance are

$$\bar{\mathbf{x}} = \langle \mathbf{x} \rangle, \quad \sigma^2(x_j) = \left\langle (x_j - \bar{x}_j)^2 \right\rangle, \quad (11)$$

where  $\langle \cdot \rangle$  denotes an average over the sampled images.

To relate fluctuations in the reconstructed image to their effect on the measured data, it is useful to express the weighted least-squares discrepancy introduced in Eq. (4) in matrix form,

$$\chi^2(\mathbf{x}) = (\mathbf{y} - \mathbf{P}\mathbf{x})^\top \mathbf{W} (\mathbf{y} - \mathbf{P}\mathbf{x}), \quad \mathbf{W} = \text{diag}\left(\frac{1}{y_i + \epsilon}\right). \quad (12)$$

Writing  $\chi^2$  in this form makes explicit the quadratic structure of the data-fidelity term and allows identification of the operator

$$\mathbf{H} \equiv \mathbf{P}^\top \mathbf{W} \mathbf{P}. \quad (13)$$

This operator corresponds to the curvature (Hessian) of the quadratic data fidelity term of the  $\chi^2$  objective and is widely used in local analyses of tomographic estimators defined through quadratic or likelihood-based reconstruction objectives [21]. It describes how small variations in the reconstructed image affect the data discrepancy in a quadratic approximation around the current solution. Directions in image space for which  $\mathbf{H}$  produces large responses correspond to variations that strongly influence the predicted projection data, while small responses correspond to variations that have little effect on the measured data [22, 23].

Let  $\delta\mathbf{x}^{(s)} = \mathbf{x}^{(s)} - \bar{\mathbf{x}}$  denote fluctuations around the ensemble mean. For each sample, the quantity  $\mathbf{H}\delta\mathbf{x}^{(s)}$  represents the data-weighted projection-backprojection response of that fluctuation. From the ensemble we compute the variance of these responses,

$$\sigma_{H\delta x}^2(j) = \left\langle (\mathbf{H}\delta\mathbf{x})_j^2 \right\rangle. \quad (14)$$

The square root,

$$\sigma_{H\delta x}(j) = \sqrt{\sigma_{H\delta x}^2(j)}, \quad (15)$$

will be referred to as the *data-visible standard deviation*, as it quantifies the component of ensemble variability that propagates through the data-weighted projection-backprojection cycle.

The maps  $\sigma^2(x_j)$  and  $\sigma_{H\delta x}(j)$  provide complementary diagnostic information. While  $\chi^2$  maps measure first-order mismatch between the mean reconstruction and the measured sinogram, they may saturate once acceptable global agreement is achieved. In contrast,  $\sigma_{H\delta x}(j)$  reflects second-order variability, capturing how fluctuations within the ensemble continue to influence the predicted data.

Regions where  $\sigma_{H\delta x}(j)$  remains elevated suggest sensitivity to modeling assumptions such as attenuation correction. Conversely, when  $\sigma_{H\delta x}(j)$  is suppressed and spatially homogeneous, the remaining variability is dominated by factors outside the modeled measurement physics.

A schematic overview of the stochastic reconstruction framework and the relationship between the measurement operator, the reconstruction space, and the ensemble sampling procedure is shown in Fig. 2.

## 2.2 Stochastic Gradient Descent

Hamiltonian Monte Carlo sampling is computationally more demanding than deterministic optimization. In practice, ensemble generation is therefore initialized from an image obtained by minimizing the  $\chi^2$  objective derived from Eq. (4). This minimization is performed using stochastic gradient descent (SGD).

Within the present framework, SGD serves primarily as an efficient initialization mechanism for the subsequent HMC sampling. It provides a deterministic point estimate located near a high-probability region of the sampling distribution, thereby reducing burn-in time and improving sampling stability.

The loss function corresponds to the negative log-likelihood (up to additive constants) and can be written as

$$\mathcal{L}_{\chi^2} = \sum_i \frac{(y_i - (\mathbf{P}\mathbf{x})_i)^2}{y_i + \epsilon}, \quad (16)$$

which is equivalent to the  $\chi^2$  discrepancy introduced earlier and  $\epsilon$  prevents numerical instability in the case of small counts. Minimization is performed using the Rectified Adam (RAdam) optimizer [24]. Gradients are computed analytically from the forward model, and non-negativity constraints are enforced to ensure physically meaningful activity estimates.

### 2.3 Validation strategy

To evaluate the proposed stochastic reconstruction framework, a hierarchical validation strategy is adopted to distinguish algorithmic performance from forward-model limitations and experimental uncertainties.

First, an idealized reconstruction scenario is considered in which projection data are generated with effectively infinite counting statistics and an idealized collimator model. In this regime the forward model closely matches the data-generating process, allowing the stochastic implementation to be benchmarked against deterministic iterative reconstruction methods. The objective of this stage is to verify that the stochastic optimization and sampling procedures converge to the same solution as established deterministic approaches when the inverse problem is well defined.

Second, progressively more realistic software phantom simulations are introduced, incorporating photon attenuation, geometric blur, and collimator response. These studies allow systematic investigation of forward-model adequacy and of the proposed data-visible ensemble diagnostic.

Third, experimental measurements obtained using an anthropomorphic neck–thyroid phantom are analyzed. These experiments provide realistic acquisition statistics together with known activity distributions, enabling quantitative validation of ensemble-based observables.

Finally, a clinical DATScan SPECT study is considered to illustrate the applicability of the framework under practical imaging conditions where ground truth is not available. In this case the ensemble is used primarily to assess forward-model consistency and to estimate the variability of clinically relevant derived quantities.

In addition to conventional global similarity measures, we employ two visual diagnostic metrics introduced in [25]: spatially resolved  $\chi^2$  maps and voxel-intensity histograms. The  $\chi^2$  maps provide a spatial representation of the mismatch between measured and predicted projection data, enabling identification of structured residuals associated with forward-model deficiencies. Intensity histograms summarize the statistical distribution of reconstructed voxel values and provide a complementary global assessment of reconstruction consistency with the expected activity distribution. Together, these metrics offer intuitive visual diagnostics that complement the ensemble-based analysis presented in the following sections.

## 3 Results and Discussion

The performance of the proposed stochastic reconstruction framework is evaluated across a sequence of increasingly realistic scenarios. We begin with an idealized software phantom benchmark to verify consistency with deterministic reconstruction methods. We then consider realistic simulation studies incorporating attenuation and system effects, followed by experimental measurements obtained with an anthropomorphic thyroid phantom. Finally, the methodology is demonstrated using clinical DATSCAN SPECT data to illustrate its behavior under practical imaging conditions.

### 3.1 Software Phantoms

Before moving into experimental data, we need a controlled environment to assess the applicability and effectiveness of our stochastic implementation. We conducted a simulation study using the GATE (Geant4 Application for Tomographic Emission) toolkit [26]. GATE enables detailed Monte Carlo modeling of particle interactions and detector responses in nuclear medicine. We used a Shepp-Logan-like structure with realistic background activity. The primary emission energy was set to 159 keV, corresponding to the photon energy of  $^{123}\text{I}$ . The sources were defined as ellipsoidal regions placed within the phantom, each assigned a specific activity. The activity levels ranged from 12 MBq down to 10 kBq across multiple regions:

- Primary sources: 12 MBq
- Intermediate sources: 325 kBq to 1 MBq
- Low-uptake regions: 10–40 kBq

This setup creates a realistic simulation scenario including attenuation and scatter, enabling comprehensive evaluation of reconstruction performance. The output sinogram data generated by this simulation serves as the input for both Hamiltonian Monte Carlo and gradient-based reconstruction methods.

*3.1.1 Idealized benchmark against deterministic reconstruction* As a first validation step, we benchmark the stochastic reconstruction framework in a controlled near-optimal regime by defining an

*Ideal Image* (and corresponding *Ideal Sinogram*) for the Shepp–Logan software phantom [25]. Following the standardized image taxonomy proposed in [25], the Ideal Image is not identical to the Source phantom; rather, it represents the best physically achievable reconstruction under asymptotic acquisition conditions.

In this configuration, the forward model retains the irreducible physics of photon transport (attenuation and scatter) while suppressing avoidable instrumental and statistical limitations such as finite counting statistics, detector blur, and collimator-induced degradation. This is implemented by simulating very high counting statistics and adopting an ideal collimator (software collimation), ensuring geometrically perfect ray acceptance. Under these conditions, remaining discrepancies reflect intrinsic transport physics rather than reconstruction artifacts.

Stochastic gradient descent (SGD) was used to minimize the  $\chi^2$  objective (Eq. 16) using the RAdam optimizer with non-negativity constraints. For comparison, reconstruction using Maximum Likelihood Expectation Maximization (MLEM) was also performed under identical forward-model assumptions. The resulting reconstructions and corresponding local  $\chi^2$  maps (introduced in [25]) are shown in Fig. 3.

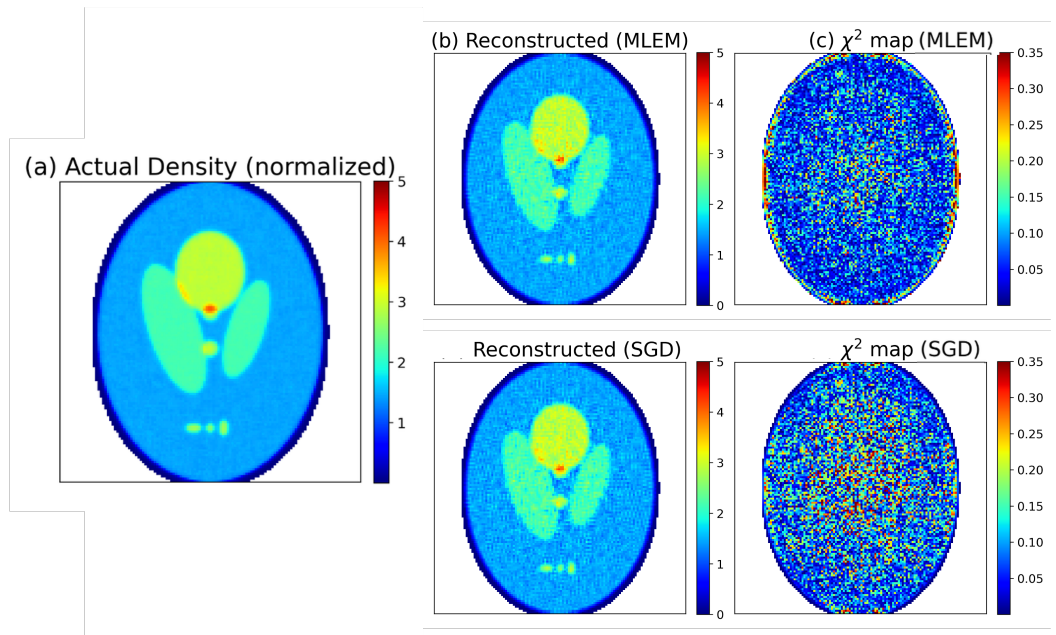


Figure 3: (a) True activity distribution (normalized). (b) MLEM reconstruction and corresponding local  $\chi^2$  map. (c) SGD reconstruction and corresponding local  $\chi^2$  map. Both methods converge to visually and statistically comparable solutions under idealized conditions. The  $\chi^2$  map metric is analyzed in detail in [25].

Comparison with MLEM demonstrates that both approaches converge to statistically indistinguishable solutions in the ideal limit. Histograms of voxel intensities (Fig. 4) and quantitative metrics (Table 1) confirm agreement across MSE, MAE, PSNR, and SSIM.

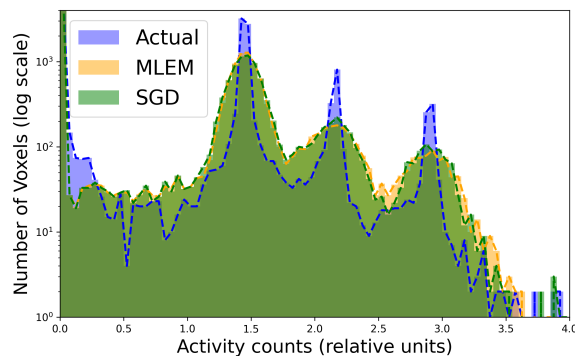


Figure 4: Voxel-intensity histograms for the true image (blue), MLEM (orange), and SGD (green). This metric is analyzed in detail in [25].

Table 1: Reconstruction quality metrics (mean  $\pm$  std).

Metric	MLEM	SGD
MSE	0.01039 $\pm$ 0.00065	0.00986 $\pm$ 0.00062
MAE	0.06266 $\pm$ 0.00155	0.06213 $\pm$ 0.00153
PSNR	29.82 $\pm$ 0.01	31.64 $\pm$ 0.01
SSIM	0.99358 $\pm$ 0.00781	0.99392 $\pm$ 0.00780

These results establish that, in the absence of hardware limitations and statistical noise, the stochastic formulation and deterministic MLEM converge to the same solution determined by the common forward model and likelihood. The stochastic formulation therefore does not alter the optimal reconstruction, but instead provides access to an ensemble of solutions in the vicinity of that optimum. The purpose of the stochastic framework is thus not improved point-estimate accuracy in this idealized limit, but the additional ensemble-based insight that becomes relevant under realistic acquisition conditions.

*3.1.2 Realistic simulation with attenuation and scatter* The mean reconstructions obtained with Hamiltonian Monte Carlo (HMC) are comparable to those produced by stochastic gradient descent (SGD) and deterministic MLEM methods. The primary objective of HMC in the present work, however, is not improved point estimation but the extraction of physically interpretable fluctuation structure from the generated ensemble.

HMC produces an ensemble of statistically consistent reconstructed images sampled from the distribution  $e^{-\chi^2/2}$ . Each sample represents a plausible activity distribution compatible with the measured data and the assumed forward model. Expectation values of arbitrary observables can therefore be evaluated directly as ensemble averages.

To evaluate the framework under realistic imaging conditions, we constructed a fully three-dimensional voxelized software phantom and simulated the complete SPECT acquisition chain using the GATE Monte Carlo toolkit. Forward projections were generated with full photon-transport modeling, including attenuation and collimator effects. This three-dimensional validation is essential because subsequent sections use voxelized attenuation maps derived from experimental measurements, requiring methodological consistency.

Unlike the idealized benchmark, the present scenario incorporates attenuation, geometric blur, and realistic collimator response. Reconstruction accuracy is therefore reduced relative to the ideal case. The goal here is not to optimize image quality per se, but to examine whether ensemble-based diagnostics can distinguish intrinsic physics limitations from forward-model deficiencies.

Three attenuation configurations were considered:

- **Model 1:** uniform attenuation with an ideal collimator assumption.
- **Model 2:** attenuation correction combined with a realistic collimator model.
- **Model 3:** incomplete attenuation correction using an exponentially decreasing attenuation coefficient.

Introducing uniform attenuation correction (Model 1) substantially reduces large-scale structured residuals in the  $\chi^2$  map. With further refinement in Model 2, which incorporates realistic collimator response, residuals become largely noise-like. At this stage, visual inspection of  $\chi^2$  alone provides limited additional spatial discrimination because structured misfit patterns are largely suppressed.

In contrast, the sampled data-visible variance  $\sigma(H\delta x)$  reveals a clear progression with model refinement. From NC to Model 1 and from Model 1 to Model 2,  $\sigma(H\delta x)$  decreases and becomes increasingly homogeneous within the object. This behavior indicates that fluctuations project less strongly into data-sensitive directions and that the remaining variability is dominated by intrinsically weakly constrained modes of the inverse problem.

Model 3 intentionally introduces attenuation mismatch through a depth-dependent under-correction. As shown in Fig. 5, this produces renewed structure in the  $\chi^2$  map, indicating forward-model inconsistency. Although the mean reconstruction remains visually similar to Models 1–2, the sampled  $\sigma(H\delta x)$  map increases relative to Model 2 and regains a pronounced spatial gradient. While  $\chi^2$  already reflects the discrepancy,  $\sigma(H\delta x)$  provides complementary information by quantifying how ensemble fluctuations propagate through the measurement operator. Model 3 therefore serves as a controlled stress test demonstrating the sensitivity of ensemble diagnostics to attenuation-model mismatch.

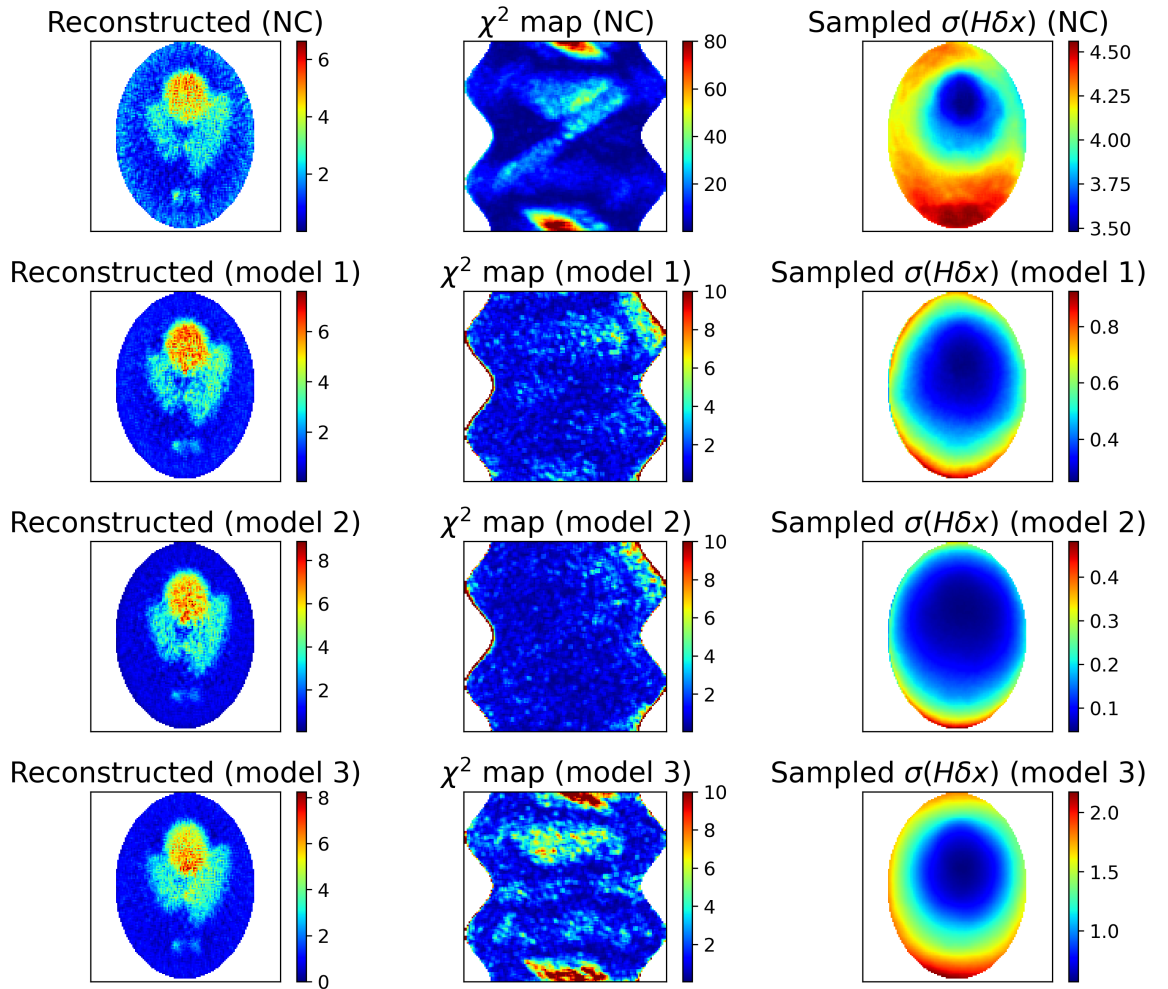


Figure 5: Application of the HMC framework to a realistic 3D voxelized software phantom. Left column: mean reconstruction. Middle column: spatially resolved  $\chi^2$  map. Right column: sampled data-visible variance  $\sigma(H\delta x)$ . Rows correspond to forward-model configurations: NC; Model 1 (uniform attenuation, ideal collimator); Model 2 (attenuation correction with realistic collimator); Model 3 (incomplete attenuation correction). Structured residuals are progressively suppressed from NC to Model 2, after which  $\chi^2$  becomes largely noise-like. In contrast,  $\sigma(H\delta x)$  decreases and homogenizes with model refinement, while Model 3 reintroduces spatially structured variance, demonstrating sensitivity to attenuation-model mismatch. All  $\sigma(H\delta x)$  maps are normalized by the mean reconstructed activity within the object mask (dimensionless).

These effects cannot be inferred from reconstructed images alone. The ensemble-based HMC framework therefore provides a practical diagnostic tool for separating physics-imposed limitations from forward-model inadequacy through spatial analysis of ensemble fluctuations.

Up to this point, the evaluation has focused primarily on qualitative diagnostics derived from voxel-wise residual and variance maps. In the following subsection we extend the analysis to quantitative measurements extracted directly from the ensemble. By evaluating physically meaningful observables—such as lesion-to-lesion activity ratios—together with their associated uncertainties, we demonstrate how ensemble-based reconstruction enables statistically grounded model comparison beyond visual assessment alone.

### 3.2 Application to an Anthropomorphic Phantom

To demonstrate the practical relevance of the proposed Hamiltonian Monte Carlo (HMC)-based reconstruction and uncertainty quantification framework, we apply it to an anthropomorphic neck-thyroid phantom designed for postsurgical SPECT/CT imaging. The phantom, introduced and characterized in detail by Michael *et al.* [27, 28], incorporates anatomically realistic structures and tissue-equivalent materials.

The phantom consists of a modular neck geometry manufactured using a combination of 3D

printing and molding techniques. It includes thyroid remnant inserts with known volumes ranging from approximately 0.5 mL to 10 mL, positioned at clinically realistic locations. Surrounding anatomical structures such as the trachea, oesophagus, cervical spine, and clavicles are also represented. The activity distribution within the phantom can be controlled to emulate realistic background-to-remnant uptake ratios, allowing systematic investigation of small-volume quantification under challenging imaging conditions.

This design enables controlled validation of reconstruction accuracy in the presence of partial-volume effects, limited spatial resolution, photon attenuation, and scatter, which are known to degrade conventional deterministic volume estimation methods.

*3.2.1 Forward Model Hierarchy and Diagnostic Objective* The experimental acquisitions were used primarily to demonstrate how HMC can serve as a diagnostic tool for forward-model assessment, rather than to optimize reconstruction accuracy. The objective is to evaluate how successive refinements of the forward model affect the consistency between measured projections and reconstructed images, and to determine the spatial origin of the remaining uncertainty.

We consider three forward modeling configurations of increasing physical realism:

1. **Geometric model (NC):** a purely geometric projection operator that neglects photon attenuation.
2. **GATE homogeneous attenuation model (Model 1):** attenuation correction implemented in GATE assuming a homogeneous water-equivalent attenuation medium. This model includes detailed photon transport and collimator response but does not account for spatial variations in tissue attenuation.
3. **Macroscopic non-uniform attenuation model (Model 2):** a computationally efficient forward model implemented in Python, incorporating spatially varying attenuation coefficients derived from the experimentally provided attenuation map. This model includes macroscopic photoelectric absorption and Compton scattering but does not explicitly simulate collimator physics. This complementary modeling structure allows partial disentanglement of transport realism (collimator response) from spatial attenuation heterogeneity, although neither model is strictly complete.

The GATE-based model therefore improves physical realism through accurate transport and collimator modeling but assumes spatially uniform attenuation. In contrast, the macroscopic model introduces spatial heterogeneity in attenuation while remaining computationally lightweight. This complementary modeling structure allows us to separate the impact of transport realism from that of spatial attenuation heterogeneity.

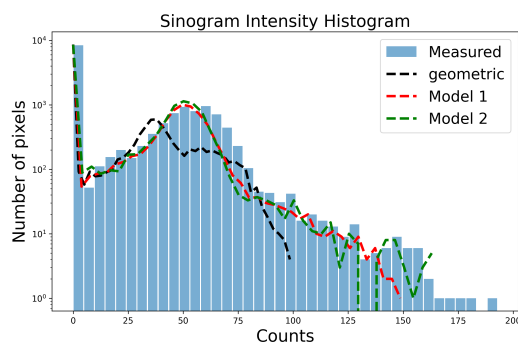


Figure 6: Sinogram intensity histograms comparing measured projection data with projections predicted by different forward models. The purely geometric model (black dashed line) shows substantial discrepancy with the measured data. Introducing attenuation correction using a homogeneous water-equivalent medium in GATE (red dashed line, Model 1) improves agreement across a broad range of count levels. Further refinement is observed when a non-uniform attenuation model derived from the experimental attenuation map is used (green dashed line, Model 2). While these histograms demonstrate progressive global improvement, they do not reveal the spatial origin of the remaining discrepancies.

Figure 6 shows that global agreement between measured and predicted sinograms improves as model complexity increases. However, histogram-based metrics remain intrinsically global and cannot

determine whether improvements affect data-constrained components of the solution or merely alter weakly constrained directions of the inverse problem.

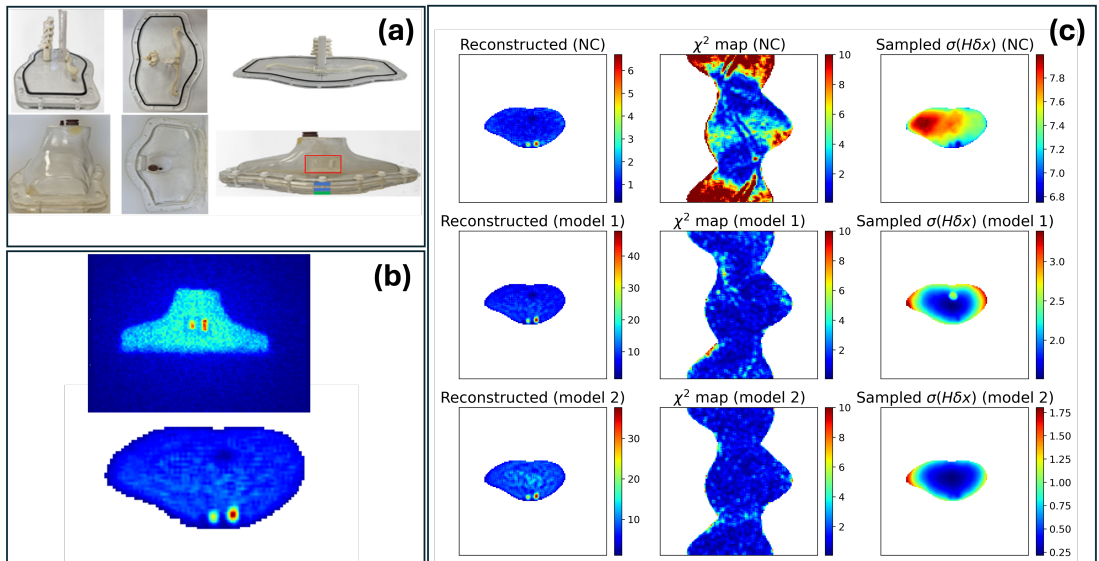


Figure 7: Application of the HMC framework to the thyroid phantom experiment. Panel (a) shows photographs of the experimental thyroid phantom. Panel (b) displays a representative detector projection (top) and the corresponding reconstructed central slice (bottom) used for the analysis. Panel (c) presents the reconstruction analysis. Each row corresponds to a different forward model. Left column: reconstructed central slice (ensemble mean). Middle column: spatially resolved  $\chi^2$  map comparing measured and predicted sinograms. Right column: sampled data-visible variance  $\sigma(H\delta x)$ . Top row (NC): geometric projection model without attenuation correction. Second row (Model 1): GATE-based simulation using a homogeneous water-equivalent attenuation model and collimator response. Third row (Model 2): macroscopic non-uniform attenuation model with spatially varying attenuation coefficients optimized from the experimental data.

While global  $\chi^2$  decreases with progressive model refinement, the  $\chi^2$  maps become increasingly noise-like, limiting their spatial diagnostic value. In contrast, the sampled  $\sigma(H\delta x)$  maps provide a clearer indication of how image fluctuations project into data-sensitive directions. The non-uniform attenuation model produces a marked suppression of  $\sigma(H\delta x)$  near object boundaries, demonstrating that forward-model improvements primarily affect regions where attenuation heterogeneity is most significant, while the bulk variability remains largely governed by intrinsic ill-posedness and counting statistics. The  $\sigma(H\delta x)$  maps are shown normalized by the mean reconstructed activity within the object mask (dimensionless, relative to image mean).

**3.2.2 HMC-Based Spatial Diagnostic** To obtain spatially resolved insight, HMC sampling is applied to each forward-model configuration. The resulting ensemble enables computation of voxel-wise variability and of the data-visible variance  $\sigma(H\delta x)$ , which quantifies how strongly image fluctuations project into data-sensitive directions defined by the measurement operator.

As shown in Fig. 7, the geometric model produces structured  $\chi^2$  residuals, indicating significant forward-model mismatch. The introduction of homogeneous attenuation correction in GATE reduces these discrepancies, although residual structure remains, consistent with unmodeled spatial heterogeneity.

The macroscopic non-uniform attenuation model further suppresses structured residuals, particularly near boundaries where attenuation gradients are strongest. Importantly, the  $\sigma(H\delta x)$  maps provide a clearer spatial demonstration of this improvement. For the refined model,  $\sigma(H\delta x)$  is markedly reduced in regions where attenuation modeling is most critical, while the remaining variability in the bulk appears comparatively uniform. This behavior indicates that residual variability is increasingly dominated by intrinsically weakly constrained modes of the inverse problem rather than by forward-model inadequacy.

Such distinctions cannot be extracted from reconstructed images,  $\chi^2$  maps, or global sinogram statistics alone. The ensemble-based HMC framework therefore provides a physically interpretable separation between modeling error and fundamental inverse-problem limitations, offering a practical tool for forward-model validation in experimental imaging studies.

*3.2.3 Quantitative lesion-to-lesion ratio (thyroid phantom)* To complement the visual residual and variance maps, we extracted a simple quantitative observable from the image ensemble: the ratio of mean reconstructed intensity between the two hot inserts of the thyroid phantom. For the acquisition ID analyzed here (ID 8 in Table 1 of [27]), the two lesions were prepared with approximately equal activity concentration ( $A_1/V_1 \approx A_2/V_2$ ), hence the expected concentration ratio is  $R_{\text{true}} \approx 1$ . The lesion sizes are close to the intrinsic spatial resolution of SPECT, placing the measurement near the partial-volume and resolution limits of the system.

Once the ensemble  $\{x^{(s)}\}_{s=1}^{N_s}$  is available, any observable that can be expressed as a function of the reconstructed image may be evaluated sample-wise and assigned an uncertainty directly from the ensemble distribution. The reliability of this uncertainty estimate depends on the adequacy of the forward model and the statistical convergence of the sampling process.

For each attenuation-model configuration (NC, Model 1, Model 2), two circular ROIs were defined around the lesion locations on each axial slice. The ROI radius  $r$  was varied to assess robustness with respect to ROI definition. For a fixed radius  $r$ , the mean ROI intensity for lesion  $\ell \in \{1, 2\}$  was estimated per sample as a variance-weighted average,

$$\mu_\ell^{(s)}(r) = \frac{\sum_{j \in \Omega_\ell(r)} w_j x_j^{(s)}}{\sum_{j \in \Omega_\ell(r)} w_j}, \quad w_j = \frac{1}{\widehat{\text{Var}}(x_j) + \epsilon}, \quad (17)$$

where  $\Omega_\ell(r)$  denotes the set of voxels inside the circular ROI (aggregated over the included axial slices),  $\widehat{\text{Var}}(x_j)$  is the sample variance estimated from the ensemble, and  $\epsilon$  prevents numerical instability.

The lesion-to-lesion ratio was then computed for each sample,

$$R^{(s)}(r) = \frac{\mu_2^{(s)}(r)}{\mu_1^{(s)}(r)}, \quad (18)$$

and summarized by the mean and standard deviation,

$$\bar{R}(r) = \langle R^{(s)}(r) \rangle, \quad \sigma_R(r) = \text{std}(R^{(s)}(r)). \quad (19)$$

This sample-wise ratio automatically incorporates covariance between the two ROI means, since it is evaluated prior to ensemble averaging.

The specific ROI construction adopted here is not essential; alternative segmentation strategies (e.g. threshold-based or Otsu-type methods) could be used equivalently. The purpose of this example is not to introduce a new segmentation methodology, but to demonstrate that once an ensemble is available, any chosen observable can be computed together with a well-defined uncertainty.

Figure 8 shows  $\bar{R}(r)$  as a function of ROI radius for the three forward-model configurations. The estimates exhibit a clear plateau over a broad range of radii, indicating stability with respect to ROI choice and demonstrating that the measurement does not rely on ad hoc thresholding. Moreover, the inter-model spread decreases as the attenuation model is refined (NC  $\rightarrow$  Model 1  $\rightarrow$  Model 2), and the estimates converge toward the expected value  $R_{\text{true}} = 1$ . This behaviour indicates that improved forward modeling enhances quantitative consistency while the ensemble naturally provides an uncertainty bound reflecting the combined effects of counting statistics and inverse-problem ambiguity.

### 3.3 Application to clinical data

To illustrate the applicability of the proposed framework to clinical data, we processed a DATSCAN SPECT study (I-123 radiopharmaceutical) of a patient diagnosed with Parkinson's disease, for which no CT-based attenuation map was available. In the absence of patient-specific attenuation information, a preliminary reconstruction was first performed without attenuation correction (NC). Subsequently, homogeneous attenuation models were introduced to approximate photon attenuation effects, including photoelectric absorption and Compton scattering.

Previous investigations have examined the role of attenuation correction (AC) in I-123-ioflupane (DATSCAN) SPECT, particularly in relation to quantitative accuracy and diagnostic performance. CT-based AC has been shown to systematically modify striatal uptake ratios and reduce bias associated with photon attenuation in the skull and soft tissues [29]. While such corrections improve quantitative consistency and anatomical plausibility, their impact on visual diagnostic classification is generally moderate. Similarly, Bienkiewicz et al. reported that CT-based AC alters quantitative binding ratios and may slightly improve diagnostic discrimination between extrapyramidal syndromes, although the effect on overall clinical categorization remains limited [30]. More recent quantitative

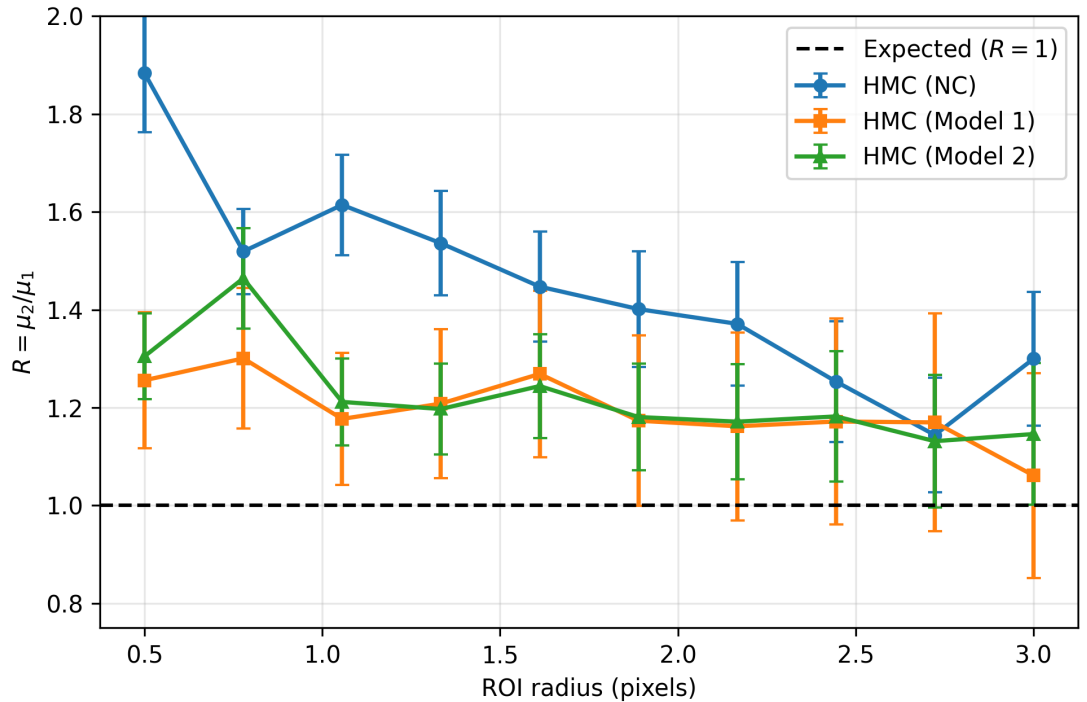


Figure 8: Ensemble-based quantitative assessment from the thyroid phantom. For each ROI radius  $r$ , the lesion-to-lesion mean-intensity ratio  $R(r) = \mu_2(r)/\mu_1(r)$  was computed sample-wise from the HMC ensemble using variance-weighted ROI means (Eq. 17) and summarized by the mean and standard deviation (Eq. 19). Error bars represent the standard deviation of  $R(r)$ . The dashed line indicates the expected concentration ratio  $R_{\text{true}} = 1$ . The plateau behaviour demonstrates robustness with respect to ROI radius, while convergence toward  $R_{\text{true}}$  and reduced inter-model spread with improved attenuation modeling indicate enhanced quantitative consistency. This example illustrates how ensemble-based reconstruction enables estimation of derived observables together with statistically consistent uncertainty bounds.

workflows employing automated threshold-based analysis tools, such as DaTQUANT, further indicate that attenuation correction contributes to improved reproducibility and calibration of quantitative metrics when standardized uptake thresholds are applied [31].

Collectively, these studies suggest that attenuation correction enhances quantitative fidelity but does not necessarily produce large changes in clinical classification. In this context, the clinical DATSCAN study presented here is not intended to evaluate diagnostic performance per se, but rather to demonstrate how an ensemble-based Hamiltonian Monte Carlo (HMC) reconstruction framework can provide a physics-grounded assessment of forward-model adequacy. By analyzing image fluctuations and their projection into data-sensitive directions through the operator  $H = P^T W P$ , the proposed approach allows evaluation of whether successive attenuation refinements meaningfully reduce data-constrained variability, thereby offering a complementary perspective beyond conventional residual or histogram-based comparisons.

In addition to the purely geometric projection model (NC), two attenuation configurations were examined. Model 1 assumes a homogeneous water-equivalent attenuation medium. Model 2 augments this homogeneous model by including a skull component, thereby introducing a simple two-region attenuation description.

At the sinogram level, as qualitatively indicated by the spatially resolved  $\chi^2$  maps (Fig. 9), the differences between the attenuation configurations are subtle and largely noise-like. In such clinical settings, where ground truth is not available and residual maps provide limited spatial guidance, it is difficult to determine whether modifications of the attenuation model lead to meaningful improvements in the reconstruction.

The sampled data-visible variance  $\sigma(H\delta x)$  provides a more structured diagnostic. The introduction of a homogeneous attenuation model modifies the spatial distribution of  $\sigma(H\delta x)$  relative to the purely geometric case. However, further refinement within the class of simple homogeneous attenuation models does not produce a systematic reduction of this quantity. This behavior suggests that the dominant sources of variability in this clinical dataset are not controlled primarily by attenuation

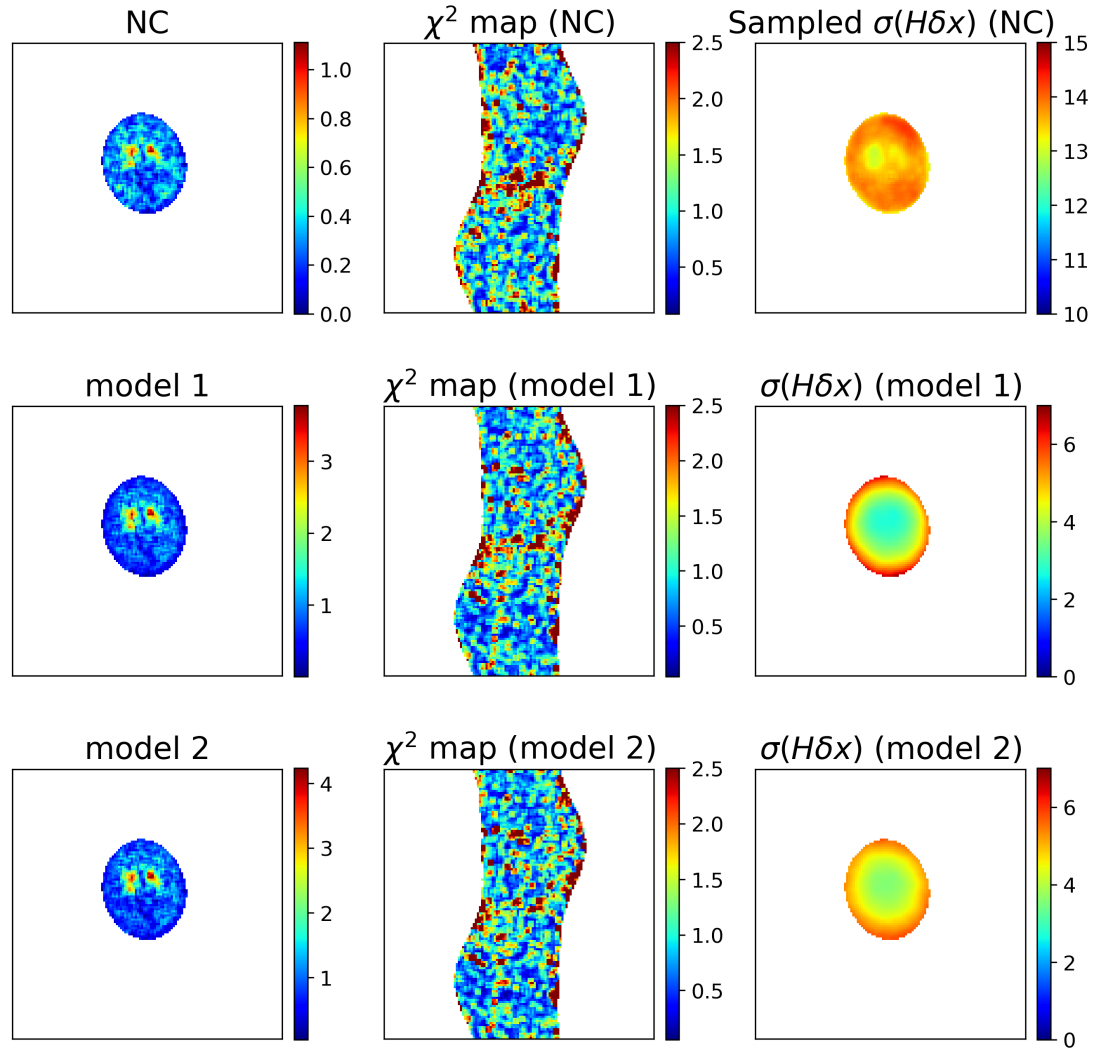


Figure 9: Application of the HMC framework to a clinical DATSCAN SPECT study. Each row corresponds to a different forward-model configuration. Left column: reconstructed central slice (ensemble mean). Middle column: spatially resolved  $\chi^2$  map comparing measured and predicted sinograms. Right column: sampled data-visible variance  $\sigma(H\delta x)$ . Top row (NC): geometric projection without attenuation correction. Middle row (Model 1): homogeneous water-equivalent attenuation model. Bottom row (Model 2): homogeneous water-equivalent attenuation model augmented with a skull component. While the  $\chi^2$  maps exhibit largely noise-like residual structure with limited distinction between models, the  $\sigma(H\delta x)$  maps provide a clearer spatial diagnostic of variability. The absence of systematic suppression of  $\sigma(H\delta x)$  across these attenuation refinements suggests that further improvement requires investigation of additional forward-model components beyond simple homogeneous attenuation modeling. The higher overall magnitude of  $\sigma(H\delta x)$  compared with the controlled phantom studies reflects the absence of patient-specific attenuation information and the increased modeling uncertainty inherent to clinical data.

scaling alone, but instead arise from other components of the imaging chain.

In this sense, the ensemble-based analysis remains informative even when variance does not decrease substantially: it indicates that further refinement of homogeneous attenuation models yields limited benefit and that improvements may require investigation of additional forward-model components, such as patient-specific attenuation maps, depth-dependent collimator response, scatter modeling beyond simple approximations, detector resolution effects, or improved noise models. The proposed ensemble-based metrics therefore provide a practical means of identifying when refinement of a particular forward-model component yields diminishing returns in clinical reconstructions.

*3.3.1 Quantitative striatal binding ratio from ensembles (clinical DATSCAN)* To complement the qualitative residual and variance diagnostics of Fig. 9, we extracted a clinically relevant quantitative

observable from the image ensemble: the striatal binding ratio (SBR), defined relative to a posterior occipital reference region. DATSCAN acquisitions are frequently assessed using striatal-to-reference uptake ratios to summarize dopaminergic transporter binding, and the present analysis uses this ratio as an illustrative example of ensemble-based quantification under low-count clinical conditions.

Given an HMC ensemble  $\{x^{(s)}\}_{s=1}^{N_s}$  and binary masks for the left striatum  $\Omega_L$ , right striatum  $\Omega_R$ , and reference region  $\Omega_{\text{ref}}$ , we compute sample-wise mean intensities

$$\mu_k^{(s)} = \frac{1}{|\Omega_k|} \sum_{j \in \Omega_k} x_j^{(s)}, \quad k \in \{L, R, \text{ref}\}, \quad (20)$$

and the corresponding sample-wise binding ratios

$$\text{SBR}_L^{(s)} = \frac{\mu_L^{(s)} - \mu_{\text{ref}}^{(s)}}{\mu_{\text{ref}}^{(s)}}, \quad \text{SBR}_R^{(s)} = \frac{\mu_R^{(s)} - \mu_{\text{ref}}^{(s)}}{\mu_{\text{ref}}^{(s)}}. \quad (21)$$

The point estimate and uncertainty are then obtained directly from the ensemble:

$$\overline{\text{SBR}}_k = \langle \text{SBR}_k^{(s)} \rangle, \quad \sigma_{\text{SBR},k} = \text{std}(\text{SBR}_k^{(s)}), \quad k \in \{L, R\}. \quad (22)$$

This procedure illustrates a general principle: once an ensemble of reconstructed images is available, any image-derived observable can be evaluated sample-wise and reported with an uncertainty estimated from the ensemble distribution. The reliability of this uncertainty depends on the adequacy of the assumed forward model and the convergence of the sampling process.

To assess robustness with respect to ROI definition, the reference ROI was systematically expanded by a fractional factor while remaining constrained to the brain mask, and the SBR was recomputed for each expansion. Figure 10 shows the resulting SBR trends for two forward-model configurations (NC and AC). In this low-count clinical setting, the uncertainty bars remain substantial, reflecting the combined effects of counting statistics, limited spatial resolution, and inverse-problem ambiguity. Nevertheless, the ensemble-based approach provides quantitative estimates with principled error bars, enabling interpretable model-to-model comparisons and supporting downstream population analyses where uncertainty propagation is essential.

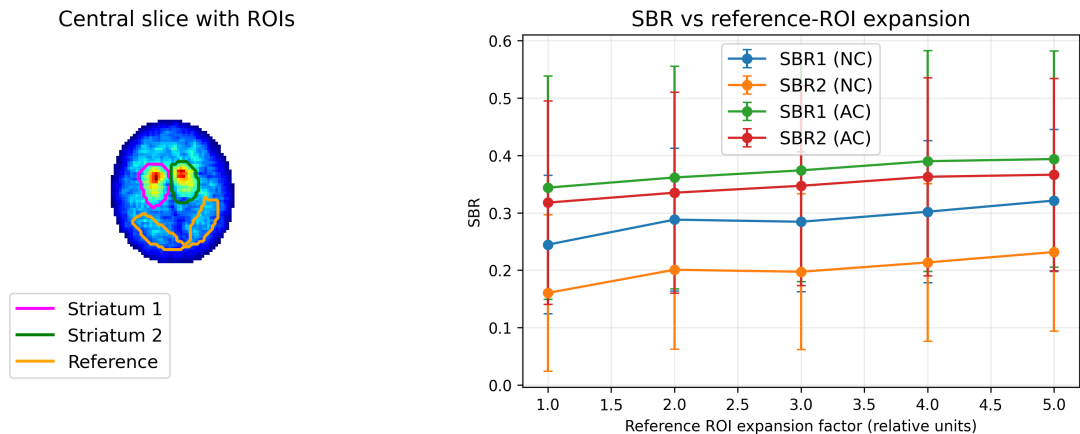


Figure 10: Quantitative striatal binding ratio (SBR) analysis for the clinical DATSCAN study. **Left:** central reconstructed slice (ensemble mean) with manually defined regions of interest (ROIs). The two upper ROIs correspond to the left and right striatal uptake regions, while the lower posterior ROI defines the reference region used for SBR normalization. **Right:** SBR estimates as a function of the fractional expansion of the reference ROI used to test robustness with respect to ROI definition. For each configuration, SBR values are computed sample-wise from the HMC ensemble according to Eq. (21), and the error bars represent the standard deviation across the sampled images. Results are shown for reconstructions without attenuation correction (NC) and with homogeneous attenuation correction (AC). While the absolute SBR values depend moderately on the reference ROI size, the estimates remain relatively stable across a broad range of expansion factors. The substantial uncertainty bars reflect the low-count clinical acquisition and the absence of patient-specific attenuation information. This example illustrates how ensemble-based reconstruction enables reporting clinically relevant uptake ratios together with uncertainty estimates derived directly from the sampled image ensemble.

### 3.4 Discussion

The results presented in this work demonstrate that the stochastic reconstruction framework based on Hamiltonian Monte Carlo (HMC) sampling can be applied practically to voxel-based emission tomography problems and can provide information that is not accessible through conventional point-estimate reconstruction methods. While deterministic approaches such as MLEM or gradient-based optimization aim to produce a single reconstructed image, the ensemble generated by HMC represents a statistical description of the set of images compatible with the measured projection data and the assumed forward model.

Under controlled conditions, the stochastic reconstruction was shown to converge to solutions that are statistically consistent with deterministic methods. In the idealized benchmark study using the software phantom, both stochastic gradient descent (SGD) and MLEM reconstructions produced images with comparable quantitative metrics, confirming that the stochastic formulation does not alter the underlying solution defined by the forward model and likelihood. In this regime the principal role of HMC is therefore not improved point-estimate accuracy, but the characterization of the distribution of solutions around the reconstructed image.

The ensemble structure becomes particularly informative when realistic acquisition conditions and modeling imperfections are introduced. The sampled data-visible variance,  $\sigma(H\delta x)$ , provides a spatially resolved diagnostic that quantifies how fluctuations propagate through the data-weighted projection-backprojection operator  $H = P^T W P$ . This quantity isolates the component of uncertainty that remains coupled to the measured data and therefore provides insight into the conditioning of the inverse problem under the assumed forward model. Across the software phantom and experimental phantom studies, improvements in the forward model were reflected not only in reduced residual structure in the  $\chi^2$  maps but also in a systematic reduction and homogenization of  $\sigma(H\delta x)$  within the object. This behavior indicates that fluctuations increasingly project into weakly constrained directions of the inverse problem rather than into data-sensitive modes.

An important observation is that the spatial structure of  $\sigma(H\delta x)$  can reveal forward-model deficiencies even when reconstructed images or residual maps appear visually acceptable. In the controlled simulation where an intentionally incomplete attenuation model was introduced, the mean reconstruction remained visually similar to that obtained with more accurate models, while the  $\sigma(H\delta x)$  maps exhibited clear spatial structure reflecting the model mismatch. This demonstrates that ensemble-based diagnostics can provide complementary information beyond conventional reconstruction evaluation metrics.

The application to the anthropomorphic thyroid phantom further illustrates the practical use of image ensembles for quantitative measurements. Because observables can be evaluated sample-wise over the ensemble, derived quantities such as lesion-to-lesion activity ratios can be estimated together with uncertainty bounds derived directly from the ensemble distribution. Importantly, these uncertainty estimates incorporate both counting statistics and the ambiguity of the inverse problem, avoiding the need for ad hoc error propagation methods.

The clinical DATSCAN example highlights the challenges associated with forward-model assessment in realistic imaging scenarios where ground truth is not available. In this case the ensemble diagnostics indicate that simple homogeneous attenuation corrections produce only limited reduction of data-constrained uncertainty, suggesting that additional components of the imaging model—such as patient-specific attenuation maps, depth-dependent collimator response, or improved scatter modeling—may be required to meaningfully improve reconstruction consistency.

Despite these advantages, the proposed stochastic framework remains computationally more demanding than conventional deterministic methods. Hamiltonian Monte Carlo requires repeated evaluation of forward and adjoint projections during the simulation of Hamiltonian trajectories, which increases computational cost relative to standard iterative reconstruction. However, the use of GPU-accelerated numerical libraries and gradient-based initialization significantly reduces the practical cost of ensemble generation, making the approach feasible on modern workstations.

Overall, the results indicate that ensemble-based stochastic reconstruction can complement existing deterministic reconstruction methods by providing a physically interpretable framework for uncertainty quantification and forward-model validation. Rather than replacing conventional algorithms, the approach can serve as an additional diagnostic layer capable of identifying the origin of residual uncertainty and guiding improvements in forward-model formulation for emission tomography.

## 4 Conclusions and Outlook

In this work we presented a stochastic formulation of the AMIAS/RISE reconstruction framework based on Hamiltonian Monte Carlo (HMC) sampling, combined with stochastic gradient descent (SGD) initialization. The use of SGD provides a fast deterministic approximation of the reconstruction

solution, enabling efficient initialization of the HMC sampling stage while maintaining computational practicality on standard GPU-enabled workstations.

Under controlled conditions, the stochastic reconstruction achieves image quality comparable to established deterministic iterative methods. The principal advantage of the approach, however, lies not in marginal improvements of point estimates but in the information contained in the ensemble of reconstructed images. The ensemble allows direct evaluation of uncertainty and provides spatially resolved diagnostics of the adequacy of the forward model.

In particular, we demonstrated that the sampled data-visible variance  $\sigma(H\delta x)$  provides a physically interpretable measure of model adequacy. Through software phantom studies, anthropomorphic phantom experiments, and a clinical DATSCAN acquisition, the ensemble analysis was shown to distinguish between uncertainty arising from the intrinsic ill-posedness of the inverse problem and uncertainty related to forward-model limitations. In practical terms, the method can indicate whether refinement of a specific component of the imaging model, such as attenuation or collimator modeling, produces a meaningful reduction of data-constrained uncertainty.

The ensemble representation also enables estimation of clinically relevant derived observables together with uncertainty estimates obtained directly from the sampled image distribution. In the DATSCAN example presented here, the ensemble was used to estimate striatal binding ratios (SBR) and their associated uncertainties under low-count clinical conditions. Such uncertainty estimates can complement existing quantitative metrics and may improve the robustness of statistical analyses in population-based imaging studies.

Within the framework of the ongoing PERSPECT project (<https://perspect.frederick.ac.cy>), the methodology presented here will be further integrated into quantitative SPECT reconstruction workflows. In combination with existing reconstruction and analysis tools, ensemble-based diagnostics are expected to provide an additional layer of validation for forward models and systematic assessment of reconstruction reliability.

More broadly, this work illustrates how modern GPU-enabled numerical frameworks make ensemble-based stochastic reconstruction practically accessible alongside traditional iterative methods such as MLEM. By combining fast deterministic optimization with Hamiltonian sampling, the proposed approach provides a practical path toward uncertainty-aware emission tomography and physics-informed model validation in realistic imaging scenarios. In clinical practice, such capabilities may contribute to more reliable quantitative measurements and improved understanding of the limitations of current imaging models when ground truth is unavailable.

### Acknowledgements

This work was supported by the Cyprus Research and Innovation Foundation under the project PERSPECT (Project No. EXCELLENCE/0524/0410). PERSPECT project is implemented in the frames of Cohesion Policy Programme “THALIA 2021-2027” and is co-funded by the European Union. In addition, this work was supported by computing time awarded on the Cyclone supercomputer of the High Performance Computing Facility of The Cyprus Institute under project “Medical Imaging” (mi).

### References

- [1] Bouchareb Y, AlSaadi A, Zabah J, Jain A, Al-Jabri A, Phiri P, Shi J Q, Delanerolle G and Sirasanagandla S R 2024 *Diagnostics* **14** ISSN 2075-4418 <https://www.mdpi.com/2075-4418/14/13/1431>
- [2] Stiliaris E and Papanicolas C N 2007 *AIP Conference Proceedings* **904** 257–268 ISSN 0094-243X <https://doi.org/10.1063/1.2734310>
- [3] Papanicolas C N and Stiliaris E 2012 *arXiv e-prints* arXiv:1205.6505 <https://ui.adsabs.harvard.edu/abs/2012arXiv1205.6505P> (Preprint 1205.6505)
- [4] Alexandrou C, Papanicolas C N and Vanderhaeghen M 2012 *Rev. Mod. Phys.* **84**(3) 1231–1251 <https://arxiv.org/abs/1201.4511>
- [5] Alexandrou C, Leontiou T, Papanicolas C N and Stiliaris E 2015 *Phys. Rev. D* **91**(1) 014506 <https://link.aps.org/doi/10.1103/PhysRevD.91.014506>
- [6] Markou L, Stiliaris E and Papanicolas C N 2018 *The European Physical Journal A* **54** 115
- [7] Koutsantonis L 2018 *The Cyprus Institute*

- [8] Papanicolas C N, Koutsantonis L and Stiliaris E 2018 A novel analysis method for emission tomography <https://arxiv.org/abs/1804.03915> (*Preprint 1804.03915*)
- [9] Koutsantonis L, Papanicolas C N and Stiliaris E 2018 Rise: A method for 3d reconstruction of spect images - validation with a hardware phantom *2018 IEEE Nuclear Science Symposium and Medical Imaging Conference Proceedings (NSS/MIC)* pp 1–5 <https://ieeexplore.ieee.org/document/8824300>
- [10] Keliri A, Koutsantonis L, Stiliaris E, Parpottas Y, Charitou G, Panagi S and Papanicolas C N 2021 Application of rise in spect myocardial perfusion imaging, using a cardiac phantom *2021 IEEE Nuclear Science Symposium and Medical Imaging Conference (NSS/MIC)* pp 1–5 <https://ieeexplore.ieee.org/document/9875921>
- [11] Lemesios C, Hadjitheodorou P, Koutsantonis L, Vrachimis A, Zamboglou N and Papanicolas C N 2021 Improved pet tomographic image reconstruction by employing the rise method *2021 IEEE Nuclear Science Symposium and Medical Imaging Conference (NSS/MIC)* pp 1–4 <https://ieeexplore.ieee.org/document/9875723>
- [12] Koutsantonis L, Rapsomanikis A N, Stiliaris E and Papanicolas C N 2019 *Infrared Physics & Technology* **98** 266–277 ISSN 1350-4495 <http://dx.doi.org/10.1016/j.infrared.2019.03.015>
- [13] Papanicolas C N, Koutsantonis L and Stiliaris E 2018 Attributing uncertainties in the identification of hotspots in spect imaging *2018 IEEE Nuclear Science Symposium and Medical Imaging Conference Proceedings (NSS/MIC)* (IEEE) p 1–5 <http://dx.doi.org/10.1109/NSSMIC.2018.8824274>
- [14] Wang G, Ye J C, Mueller K and Fessler J A 2018 *IEEE Transactions on Medical Imaging* **37** 1289–1296 <https://ieeexplore.ieee.org/document/8359079>
- [15] Apostolopoulos I D, Papandrianos N I, Feleki A, Moustakidis S and Papageorgiou E I 2023 *EJNMMI Physics* **10** 6 <https://link.springer.com/article/10.1186/s40658-022-00522-7>
- [16] Shepp L A and Vardi Y 1982 *IEEE Transactions on Medical Imaging* **1** 113–122 <https://ieeexplore.ieee.org/document/4307558>
- [17] Betancourt M 2017 *arXiv preprint* <https://arxiv.org/abs/1701.02434> (*Preprint 1701.02434*)
- [18] Neal R M 2011 Mcmc using hamiltonian dynamics *Handbook of Markov Chain Monte Carlo* ed Brooks S, Gelman A, Jones G L and Meng X L (Chapman and Hall/CRC) pp 113–162 <https://arxiv.org/abs/1206.1901>
- [19] Fichtner A, Zunino A and Gebraad L 2018 *Geophysical Journal International* **216** 1344–1363 ISSN 0956-540X <https://arxiv.org/pdf/2103.07515>
- [20] Reader A J and Verhaeghe J 2014 *Physics in Medicine & Biology* **59** R371 <https://doi.org/10.1088/0031-9155/59/22/R371>
- [21] Fessler J A 1996 *IEEE Transactions on Image Processing* **5** 493–506 <https://ieeexplore.ieee.org/document/491322>
- [22] Engl H W, Hanke M and Neubauer A 1996 *Regularization of Inverse Problems (Mathematics and Its Applications vol 375)* (Springer)
- [23] Stuart A M 2010 *Acta Numerica* **19** 451–559 <https://scispace.com/pdf/inverse-problems-a-bayesian-perspective-1dknxttxjb.pdf>
- [24] Liu L, Jiang H, He P, Chen W, Liu X, Gao J and Han J 2021 On the variance of the adaptive learning rate and beyond <https://arxiv.org/abs/1908.03265> (*Preprint 1908.03265*)
- [25] Frixou A, Leontiou T, Efstathios S and Papanicolas C N “Standardized Images and Evaluation Metrics for Tomography”, under preparation <https://arxiv.org/pdf/2601.07531>
- [26] Sarrut D and et al 2022 *Physics in Medicine & Biology* **67** 104001 <https://arxiv.org/abs/physics/0408109>

- [27] Michael K, Frangos S, Iakovou I, Lontos A, Demosthenous G and Parpottas Y 2024 *Life* **14** ISSN 2075-1729 <https://www.mdpi.com/2075-1729/14/1/113>
- [28] Michael K, Hadjiconstanti A, Lontos A, Demosthenous G, Frangos S and Parpottas Y 2023 *Life* **13** ISSN 2075-1729 <https://www.mdpi.com/2075-1729/13/4/961>
- [29] Lange C, Seese A, Schwarzenböck S, Steinhoff K, Umland-Seidler B, Krause B J, Brenner W, Sabri O, Kurth J, Hesse S and Buchert R 2014 *PLOS ONE* **9** e108328 <https://pubmed.ncbi.nlm.nih.gov/25268228>
- [30] Bieńkiewicz M, Górska-Chrzastek M, Siennicki J, Gajos A, Bogucki A, Mochecka-Thoelke A, Płachcińska A and Kuśmierk J 2008 *Nuclear Medicine Review. Central & Eastern Europe* **11** 53–58 [https://www.researchgate.net/publication/26654850\\_Impact\\_of\\_CT\\_based\\_attenuation\\_correction\\_on\\_quantitative\\_assessment\\_of\\_DaTSCAN\\_123I-Ioflupane\\_imaging\\_in\\_diagnosis\\_of\\_extrapyramidal\\_diseases](https://www.researchgate.net/publication/26654850_Impact_of_CT_based_attenuation_correction_on_quantitative_assessment_of_DaTSCAN_123I-Ioflupane_imaging_in_diagnosis_of_extrapyramidal_diseases)
- [31] Neill M, Fisher J, Brand C, Lei H, Sherman S, Chou Y H and Kuo P 2021 *Tomography* **7** 980–989 <https://www.mdpi.com/2379-139X/7/4/81>